Nanoscale

ROYAL SOCIETY OF CHEMISTRY

PAPER

View Article Online
View Journal | View Issue

Cite this: *Nanoscale*, 2025, **17**, 540

Theoretical understanding of the in-plane tensile strain effects on enhancing the ferroelectric performance of $Hf_{0.5}Zr_{0.5}O_2$ and ZrO_2 thin films†

Kun Hee Ye,[a,b] Taeyoung Jeong,[a,b] Seungjae Yoon,[a,b] Dohyun Kim,[a,b] Cheol Seong Hwang *[b] and Jung-Hae Choi *[a]

In-plane tensile strain was reported to enhance the ferroelectricity of $Hf_{1-x}Zr_xO_2$ thin films by promoting the formation of a polar orthorhombic (PO-) phase. However, its origin remains yet to be identified unambiguously, although a strain-related thermodynamic stability variation was reported. This work explores the kinetic effects that have been overlooked to provide a precise answer to the problem, supplementing the thermodynamic calculations. The in-plane strain-dependent phase fractions were identified by calculating the relative influences of the thermodynamic factor (Boltzmann distribution of free energies of polymorphs) and the kinetic factor (transition rate between polymorphs using the Johnson–Mehl–Avrami equation). The monoclinic (M-) phase constitutes the ground state under almost all conditions. However, its formation is kinetically suppressed by the high activation barrier for the transition from the tetragonal (T-) phase. In contrast, PO-phase formation is dominated by thermodynamic effects and is promoted under in-plane tensile strain due to the energetic stabilization of the PO-phase, while the T- to PO-phase transition is kinetically probable due to a low activation barrier. The in-plane tensile strain also lowers the activation barrier of T → M. Hence, the optimal tensile strain for PO-phase formation varies depending on the thermal conditions. The remanent polarization was calculated using spontaneous polarization and the PO-phase fraction. The in-plane tensile strain of 2–2.5% and moderate annealing at approximately 700 K were optimum for increasing ferroelectricity by 34% in $Hf_{0.5}Zr_{0.5}O_2$ and 106% in ZrO_2 along the ⟨111⟩ orientation.

Received 13th August 2024,
Accepted 7th November 2024

DOI: 10.1039/d4nr03333g

rsc.li/nanoscale

Introduction

Ferroelectric $Hf_{1-x}Zr_xO_2$ (HZO) thin films draw significant attention for their applications in complementary metal–oxide-semiconductor (CMOS) compatible semiconductor memory.[1,2] Ferroelectricity in HZO thin films originates from the metastable $Pca2_1$ polar orthorhombic (PO-) phase, and field-induced ferroelectric characteristics in Zr-rich HZO thin films manifest through the phase transition between the metastable $P4_2/nmc$ tetragonal (T-) phase and the PO phase.[3–6] Therefore, promoting the formation of metastable phases while suppressing the ground state $P2_1/c$ monoclinic (M-) phase is desirable for memory applications. Over the past decades, this issue has been the subject of extensive research in academia and industry, where the thin film composition and growth steps were examined. Besides, the HZO thin films on electrodes/substrates generally involve strains of diverse origins, including intrinsic growth and extrinsic thermal strains. It was recently reported that in-plane tensile strain substantially enhances ferroelectricity in HZO thin films. Kim *et al.* demonstrated that increasing in-plane tensile stress through thicker TiN electrodes enhances the remanent polarization (P_r) in polycrystalline $Hf_{0.5}Zr_{0.5}O_2$.[7] Similarly, Y. Goh *et al.* reported increasing P_r of polycrystalline $Hf_{0.5}Zr_{0.5}O_2$ under thermal tensile stress from heat treatment by adopting different electrodes.[8] An increase in ferroelectricity under tensile strain was also observed in epitaxial $Hf_{0.5}Zr_{0.5}O_2$ on (La,Sr)MnO_3.[9] Therefore, strain control is crucial in achieving high performance.

Another essential research area is the theoretical understanding of the strain effects on ferroelectricity by density functional theory (DFT) calculations. The primary target of DFT calculations is to calculate the thermodynamic free

[a]*Electronic Materials Research Center, Korea Institute of Science and Technology, Seoul 02792, Korea. E-mail: choijh@kist.re.kr; Fax: +82 2 958 6658; Tel: +822 958 5488*

[b]*Department of Materials Science and Engineering and Inter-University Semiconductor Research Center, Seoul National University, Seoul 08826, Korea. E-mail: cheolsh@snu.ac.kr; Fax: +82 2 884 1413; Tel: +822 880 7535*

† Electronic supplementary information (ESI) available. See DOI: https://doi.org/10.1039/d4nr03333g

energy of HZO polymorphs, considering the contributions from the surface energy.[10] However, the surface effects alone cannot thermodynamically stabilize the PO phase. Several recent DFT studies also considered the effects of in-plane strain on the thermodynamic stability of various polymorphs. However, the conclusions remain controversial. For example, Materlik *et al.* reported that {001} plane-oriented PO-phase $Hf_{0.5}Zr_{0.5}O_2$ could be stabilized under ~8 GPa compressive stress from their DFT study,[11] while the experimental results generally indicated destabilization under compressive stress.[12,13]

Several works reported the phase stability of ⟨111⟩ oriented HfO_2.[14–16] The M-($\bar{1}$11) and M-(111) planes were reported to be stable under in-plane compressive and tensile strain, respectively, indicating that the PO-phase formation is impossible even under strain.[14] Therefore, previous theoretical studies on the effects of in-plane strain in HZO have not fully explained the increase in ferroelectricity under in-plane tensile strain in the experiments. Such a discrepancy may arise from considering only the free energy of the HZO polymorphs and neglecting the kinetic effects of the transition between them, implying that the consideration of the transition barrier between the polymorphs is essential for understanding the formation of the PO phase under in-plane strain.

On the other hand, the authors' recent work elucidated the phase formation on the general thermal process of thin film HZO during atomic layer deposition (ALD): crystallization from amorphous → phase transition and annealing → phase transition during cooling.[17] The phase fractions were calculated using the Boltzmann distribution of thermodynamic free energy of polymorphs and the kinetic activation barrier based on the Johnson–Mehl–Avrami (JMA) equation, respectively. The quantitative phase fractions were calculated as a function of Zr content (x), annealing temperature, and grain size, consistent with the experimental results, thus validating the robustness of this methodology. Nonetheless, the strain effect has not been considered in previous studies. Therefore, this study investigates the effects of in-plane strain on the phase fractions of $Hf_{0.5}Zr_{0.5}O_2$ and ZrO_2 by taking the strain term into theoretical consideration. A comprehensive analysis of the in-plane strain-dependent free energy and activation barrier shows that the PO phase is preferred under tensile strain. In addition, optimal ranges for the in-plane tensile strain and annealing temperature are proposed where the PO-phase fraction and polarization are maximized. Therefore, this study is expected to contribute to optimizing the electrical properties of HZO through in-plane strain engineering.

Method

DFT calculations were performed by using the Vienna *Ab initio* Simulation Package (VASP)[18,19] using the local density approximation (LDA)[20,21] with Blöchl's projector augmented wave approach.[22,23] The valence electrons of Hf ($5p^6 5d^3 6s^1$), Zr ($4s^2 4p^6 4d^3 5s^1$), and O ($2s^2 2p^4$) were considered in pseudopotentials. A plane-wave basis cutoff energy of 600 eV was adopted, and k-point meshes of Γ-centered 8 × 8 × 8 were sampled for the conventional unit cell of T-, PO-, and M-phases. The lattice constants and atomic coordinates were allowed to relax until the Hellmann–Feynman forces were below 0.02 eV Å^{-1}.

To estimate the energetic stability of $Hf_{0.5}Zr_{0.5}O_2$ and ZrO_2 polymorphs under in-plane strain, the ⟨111⟩ orientations were determined as the out-of-plane direction. Biaxial in-plane strain was then applied to {111} planes, with the lattice constants and angles of in-plane directions fixed, while the out-of-plane lattice parameter and angle were allowed to relax freely. The vibration-free energies of the strained structures were calculated using phonopy *via* the finite displacement method, enabling the calculation of Helmholtz free energy.[24] The 96-atom structures (2 × 2 × 2 supercells) were used for the M- and PO-phases. In the case of the T-phase, the supercell having 216 atoms was utilized to remove the computationally generated imaginary frequency under in-plane strain. The primitive T-phase was expanded by the matrix operation of $\begin{pmatrix} 3 & 0 & 0 \\ 0 & 2 & -3 \\ 0 & 2 & 3 \end{pmatrix}$. The surface energy was computed using the slabs of 8 layers with a vacuum region thicker than 10 Å. For the slab structures, the k-point meshes of Γ-centered 6 × 6 × 1 were used. Several surface energies of the PO phase may not converge due to the polarity of the PO phase. Thus, the antipolar orthorhombic (AO-) phase, composed of two PO phases with opposite dipole moments, was employed to replace the surface energy of the PO phase. The in-plane strain-dependent spontaneous polarizations (P_s) of the PO phase were calculated through the Berry phase method by considering the polarization quantum.[25,26]

Results and discussion

In-plane strain effects on the thermodynamic free energy

The ⟨111⟩ orientations were set to the out-of-plane direction because {111} planes were reported to have the lowest surface energy in all the HZO polymorphs.[10,17,27] Fig. 1(a) shows the cell structure used in the calculations, composed of 12 Hf/Zr and 24 O atoms along the ⟨111⟩ orientation. The gray shade region has 4 cations and 8 anions and is regarded as one layer along ⟨111⟩.

Table 1 shows the lattice constants, unit cell volume (V), and bulk internal energy ($E_{i,bulk}$). The subscript i indicates a particular phase of the T-, PO-, and M-phases in $Hf_{0.5}Zr_{0.5}O_2$ and ZrO_2 – the major phases observed in experiments. Therefore, only these phases are considered in this study. Regardless of the Zr fraction, the M-phase was identified as the ground state in the equilibrium bulk state. The lattice parameters of $Hf_{0.5}Zr_{0.5}O_2$ were determined using Vegard's law between HfO_2 and ZrO_2, consistent with previous studies.[11,17]

Fig. 1(b) shows the schematic diagram showing the transition from the T- to other phases (M- or PO-phase) during

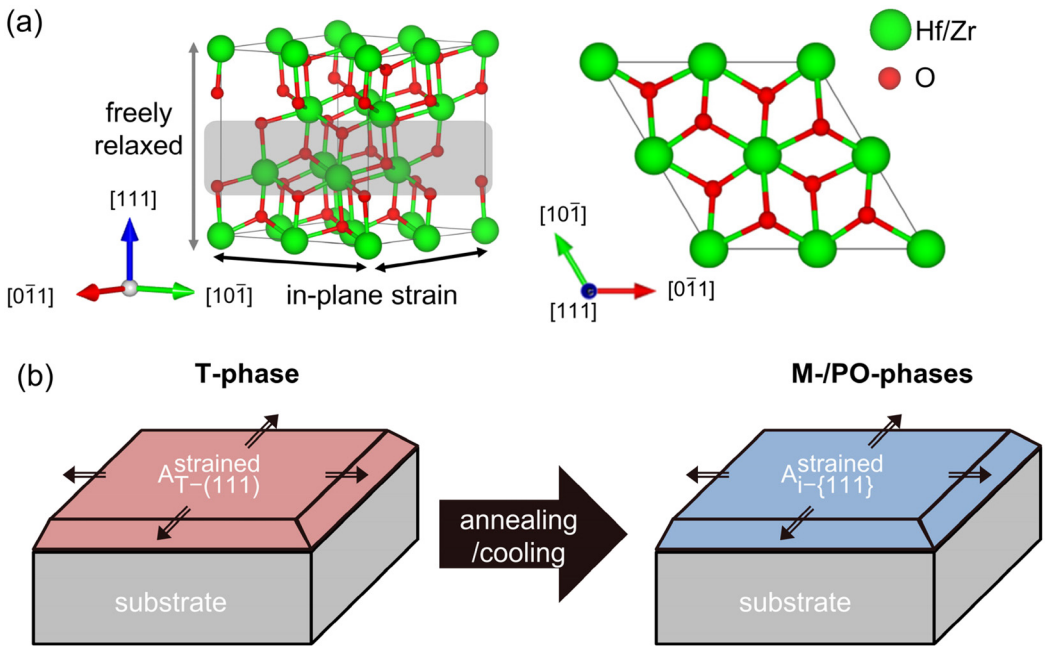

Fig. 1 (a) Atomic structure of the T-phase along the ⟨111⟩ orientation (left) and the (111) plane corresponding to the gray shade (right). (b) Schematic diagram showing the transition from the T- to any i-phase during heat treatment. The in-plane strain induced by the substrate is indicated by thin arrows and was assumed to be maintained during annealing and cooling.

Table 1 Lattice constants, unit cell volume (V), and internal energy ($E_{i,bulk}$) of T-, PO-, and M- phases in $Hf_{0.5}Zr_{0.5}O_2$ and ZrO_2. The $E_{i,bulk}$ is represented based on the T-phase as a reference

$Hf_{0.5}Zr_{0.5}O_2$	a (Å)	b (Å)	c (Å)	V (Å^3)	$E_{i,bulk}$ (meV per f.u.)
T	5.01	—	5.09	127.72	0
PO	5.19	4.99	5.01	129.60	−39
M	5.06	5.16	5.22	134.16	−83

ZrO_2	a (Å)	b (Å)	c (Å)	V (Å^3)	$E_{i,bulk}$ (meV per f.u.)
T	5.03	—	5.11	129.52	0
PO	5.22	5.02	5.03	131.77	−10
M	5.09	5.19	5.24	136.34	−49

heat treatment, representing the experimental observations. The T-phase crystallizes from amorphous $Hf_{0.5}Zr_{0.5}O_2$ and ZrO_2, so other polymorphs are formed from the T-phase after subsequent annealing and cooling steps.[10,17,28] Therefore, it was assumed that the in-plane strain of the (111) plane of the T-phase induced by the substrate remains on the {111} plane of any i-phase transformed from the T-phase. This assumption indicates that the in-plane area of the {111} plane for any i-phase ($A^{strained}_{i-111}$) remained unvaried at the value of the (111) plane of the T-phase ($A^{strained}_{T-(111)}$) even after phase transition. The in-plane strain of the {111} plane, $\varepsilon_{\{111\}}$, was determined by $A^{strained}_{i-111}$ (= $A^{strained}_{T-(111)}$) and the equilibrium in-plane area of the (111) plane of the T-phase ($A^{equil}_{T-(111)}$) was determined using eqn (1). Therefore, the strain-free state is the ground state of the T-phase in this study.

$$\varepsilon_{\{111\}} = \sqrt{\frac{A^{strained}_{i\text{-}\{111\}}}{A^{equil}_{T\text{-}(111)}}} - 1 \quad (1)$$

The $\varepsilon_{\{111\}}$ along the two orthogonal directions on the {111} plane was assumed to be identical. The $\varepsilon_{\{111\}}$ was used in all the calculations and ultimately served as the critical parameter for calculating the phase fractions throughout this study. The details on the strain conditions for all the polymorphs were investigated and are shown in Fig. S1.†

The free energy of HZO grains ($F_{i,grain}$) was calculated for all polymorphs, considering $\varepsilon_{\{111\}}$, as well as the temperature (T) and grain diameter (d_T):

$$F_{i,grain}(\varepsilon_{\{111\}}, T, d_T) = E_{i,bulk}(\varepsilon_{\{111\}}) + F_i^{vib}(\varepsilon_{\{111\}}, T) + E_{i,intf}(\varepsilon_{\{111\}}, d_T) \quad (2)$$

Eqn (2) comprises the strain-dependent internal energy ($E_{i,bulk}(\varepsilon_{\{111\}})$), free energy related to phonon vibration ($F_i^{vib}(\varepsilon_{\{111\}},T)$), and interface energy of grains ($E_{i,intf}(\varepsilon_{\{111\}},d_T)$). The $\varepsilon_{\{111\}}$ range was set to −0.025 to 0.025, following the frequently reported value in experiments.[12,29] Fig. 2(a)–(f) show each term on the right side of eqn (2) – $E_{i,bulk}$, F_i^{vib}, and $E_{i,intf}$ of the T-(111), PO-(111), M-(111), and M-($\bar{1}$11) oriented grains. Fig. 2(g) and (h) show their sum, $F_{i,grain}$, for $Hf_{0.5}Zr_{0.5}O_2$ (upper panel) and ZrO_2 (lower panel), respectively. The energies were all calculated as a function of $\varepsilon_{\{111\}}$ (lower x-axis) and $A^{strained}_{i-111}$ (upper x-axis).

Among the three energy terms, $E_{i,bulk}$ contributes the most to $F_{i,grain}$ for both $Hf_{0.5}Zr_{0.5}O_2$ and ZrO_2, as shown in Fig. 2(a) and (b), and the M-($\bar{1}$11) grain generally has the lowest $E_{i,bulk}$.

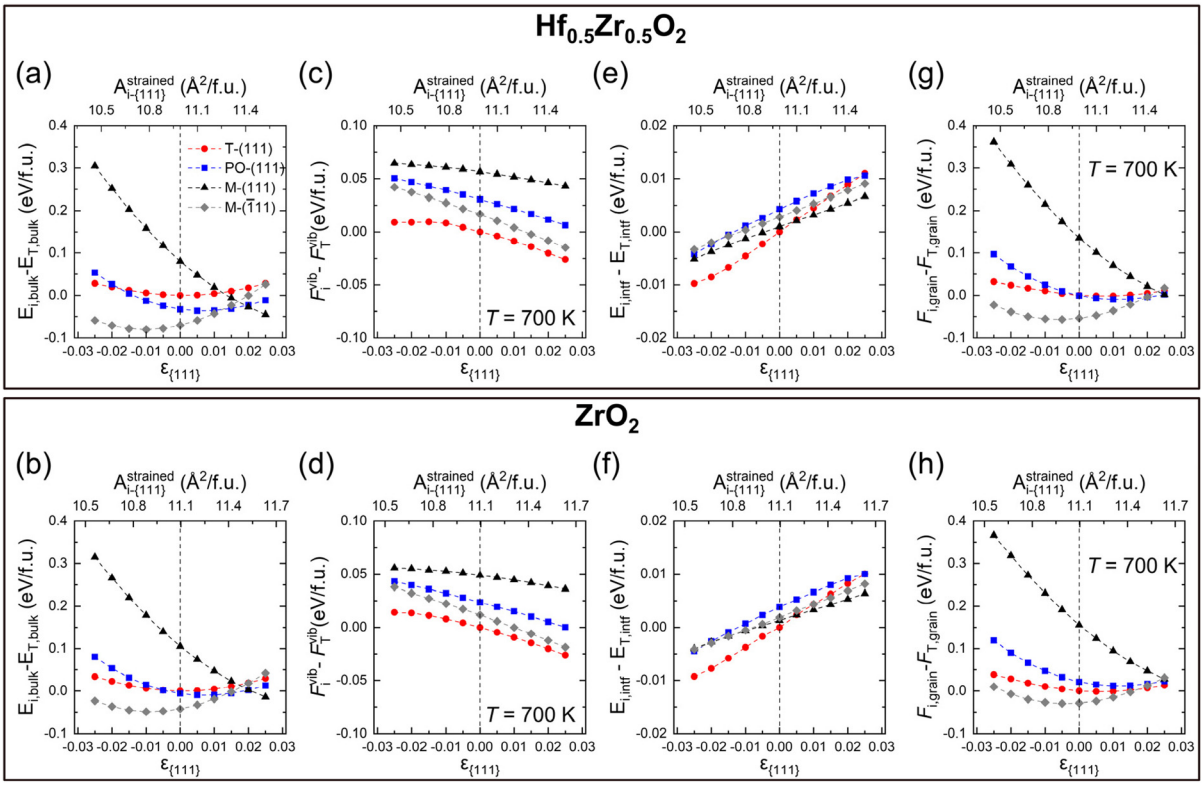

Fig. 2 Relative values of (a and b) $E_{i,bulk}$, (c and d) F_i^{vib} at 700 K, (e and f) $E_{i,intf}$, and (g and h) $F_{i,grain}$ at 700 K as a function of $\varepsilon_{\{111\}}$ (lower x-axis) and $A_{i-111}^{strained}$ (upper x-axis) for $Hf_{0.5}Zr_{0.5}O_2$ (upper panel) and ZrO_2 (lower panel), respectively. The energy of the unstrained T-phase is used as a reference. The red circle, blue square, black triangle, and gray diamond represent the T-(111), PO-(111), M-(111), and M-($\bar{1}$11) grains.

In addition, M-($\bar{1}$11) is stabilized under compressive $\varepsilon_{\{111\}}$, while M-(111) is generally favored under tensile $\varepsilon_{\{111\}}$ due to its difference in the equilibrium in-plane area, as shown in Table 2. The differences of $E_{i,bulk}$ among polymorphs are lower under tensile $\varepsilon_{\{111\}}$ rather than under compressive $\varepsilon_{(111)}$, indicating that the phase stability under tensile $\varepsilon_{\{111\}}$ might be delicately affected by other factors, such as F_i^{vib} and $E_{i,intf}$.

The F_i^{vib} values of $Hf_{0.5}Zr_{0.5}O_2$ and ZrO_2 at 700 K, the normal annealing temperature, tend to decrease slightly as $\varepsilon_{\{111\}}$ increases, as shown in Fig. 2(c) and (d). Nevertheless, their relative magnitude among the polymorphs does not change over the investigated $\varepsilon_{\{111\}}$ range. The effects of the annealing temperature on F_i^{vib} in $Hf_{0.5}Zr_{0.5}O_2$ and ZrO_2 are summarized in Fig. S2.† They commonly showed an identical tendency of gradually decreasing F_i^{vib} with increasing temperature due to phonon softening, irrespective of the phase and $\varepsilon_{\{111\}}$. Nonetheless, the F_i^{vib} of the T-phase has the lowest value, which coincides with the preference for the T-phase at high temperatures. For the F_i^{vib} calculations on the individual strained structures, only the quasi-harmonic effects were taken into account. Based on a previous report, the energy change considering the anharmonic effects was about 10^{-3} eV per f.u. for ZrO_2 at 300–700 K.[30] For $Hf_{0.5}Zr_{0.5}O_2$ polymorphs, the cation configuration was assumed to be identical to that of the primitive T-phase structure (2 Hf/Zr and 4 O atoms). It was based on the fact that the cation configuration hardly affects the mixing energy[17] and F_i^{vib} (Fig. S3 of the ESI†) in $Hf_{0.5}Zr_{0.5}O_2$.

On the other hand, the variation of $E_{i,intf}$ with $\varepsilon_{\{111\}}$ variation is an order of magnitude smaller compared to $E_{i,bulk}$ and F_i^{vib} for both $Hf_{0.5}Zr_{0.5}O_2$ and ZrO_2, as shown in Fig. 2(e) and (f). Previous studies reported that the interface energy per area ($\gamma_{i,intf}$) is calculated to be 0.33–0.5 times the surface energy.[31–34] Thus, to estimate the $\varepsilon_{\{111\}}$-dependent $E_{i,intf}$, $\gamma_{i,intf}$ was assumed to be 0.4 times the surface energy of the {111} plane ($\gamma_{i,\{111\}}$), and the $\varepsilon_{(111)}$-dependent $\gamma_{i,\{111\}}$ is shown in Fig. S4.† The film thickness was set to 10 nm and assumed to be equal to d_T, which was converted from the volume of the spherical T-phase (V_T) [$d_T = 2 \times \left(\frac{3}{4\pi} V_T\right)^{\frac{1}{3}}$]. Hence, the $E_{i,intf}(\varepsilon_{\{111\}}, d_T)$ was calculated by using the formula – $\gamma_{i,intf}$ ×

Table 2 In-plane area of the {111} plane in equilibrium state T-, PO-, and M-phases (A_{i-111}^{equil}) in $Hf_{0.5}Zr_{0.5}O_2$ and ZrO_2

	A_{i-111}^{equil} (Å^2 per f.u.)	
Phase	$Hf_{0.5}Zr_{0.5}O_2$	ZrO_2
T-(111)	10.98	11.09
PO-(111)	11.09	11.22
M-(111)	12.02	12.15
M-($\bar{1}$11)	10.75	10.87

$4\pi(d_T/2)^2$. The interface in this study includes the interface between amorphous and crystalline phases, the interface between different phases, and grain boundaries in polycrystalline structures. Since the contribution of $E_{i,intf}$ on $F_{i,grain}$ is much smaller than those of $E_{i,bulk}$ and F_i^{vib}, the effect of $E_{i,intf}$ on the phase stability will be minimal. Finally, $F_{i,grain}$ values at T = 700 K in $Hf_{0.5}Zr_{0.5}O_2$ and ZrO_2 (shown in Fig. 2(g) and (h)) show that the T-phase is stabilized in the tensile $\varepsilon_{\{111\}}$ ranges. $F_{i,grain}$ values at T = 1000 K shown in Fig. S5† also present a similar tendency.

In this study, the LDA functional was used because the average surface energy of the T-phase was calculated to be lower than that of the M-phase, which is consistent with the experimental observations.[2,3,31,35] In contrast, several studies utilized the Perdew–Burke–Ernzerhof (PBE)[10,16] or PBEsol functional.[36–38] Nevertheless, the overall bulk energetic trends were similar between the LDA and PBEsol functionals, as shown in Fig. S6.†

Fig. 3(a) and (b) show the ground state distributions of $Hf_{0.5}Zr_{0.5}O_2$ and ZrO_2 as a function of $\varepsilon_{\{111\}}$ in a temperature range of 300–1000 K when d_T is 10 nm. The red, blue, black, and gray regions indicate that the T-(111), PO-(111), M-(111), and M-($\bar{1}$11) oriented grains have the lowest $F_{i,grain}$ under the given $\varepsilon_{\{111\}}$ and temperature conditions, respectively. In both $Hf_{0.5}Zr_{0.5}O_2$ and ZrO_2, the M-($\bar{1}$11) grain was the most stable at $\varepsilon_{\{111\}}$ of −0.025 to 0.015, irrespective of the temperature. In $Hf_{0.5}Zr_{0.5}O_2$ at $\varepsilon_{\{111\}}$ of 0.02, the PO-(111) grain had the lowest $F_{i,grain}$ up to 740 K. At higher temperatures, the M-($\bar{1}$11) grain was preferred due to its lower F_i^{vib} than those of PO-(111) and M-(111) despite the high $E_{i,bulk}$ of M-($\bar{1}$11). At $\varepsilon_{\{111\}}$ of 0.025, the most stable phase changes in the following order: M-(111), PO-(111), and T-(111) as temperature increases. In ZrO_2 at $\varepsilon_{\{111\}}$ of 0.02 and 0.025, on the other hand, the PO-(111) and M-(111) grains were stable at lower temperatures, respectively, but the T-(111) grains became stabilized as the temperature increased. The variations in thermodynamic stability with temperature implied the significance of F_i^{vib}, suggesting that the annealing temperature is expected to affect the phase formation of HZO. Overall, the calculation based on the thermodynamic energy indicates that the M-($\bar{1}$11) grain is thermodynamically stable over most of the $\varepsilon_{\{111\}}$ ranges, whereas the PO-(111) grain is preferred only in a narrow range of tensile $\varepsilon_{\{111\}}$. However, the PO-phase was primarily observed in various in-plane strain ranges in experiments,[12,29] implying that the kinetic effect plays a crucial role in the phase formation of HZO.

In-plane strain effects on the kinetic activation barrier of the phase transition

This section describes the $\varepsilon_{\{111\}}$-dependent activation barrier of the phase transition to examine the kinetic effects on the transitions from the T-phase to the M- and PO-phases. Fig. 4(a) provides the schematic diagram outlining the calculation of the nucleation activation barriers of the M- or PO-phase in the T-phase ($E_{a,nuc}$(T → M) or $E_{a,nuc}$(T → PO)). Since the activation barrier for growth is significantly lower than that for nucleation,[17] only the nucleation activation barrier is considered in this study. Following the previous study, the $E_{a,nuc}$ was determined by the energy difference between the 3 × 3 × 3 supercell composed solely of the T-phase and that containing a 1 × 1 × 1 M- or PO-phase within the 3 × 3 × 3 T-phase.[17] The 3-coordinated O ions of M- and PO-phases were fixed to maintain the atomic structures. The energy profiles during the nucleation determined by the nudged elastic band method are shown in Fig. S7.†

Fig. 4(b) and (c) show the $\varepsilon_{\{111\}}$-dependent $E_{a,nuc}$(T → M) and $E_{a,nuc}$(T → PO) in $Hf_{0.5}Zr_{0.5}O_2$ and ZrO_2, respectively. In all $\varepsilon_{\{111\}}$ ranges, $E_{a,nuc}$(T → M) is significantly higher than $E_{a,nuc}$(T → PO), suggesting that the phase transition from the T-phase to the M-phase is kinetically suppressed than that to the PO-phase.

Under a tensile $\varepsilon_{\{111\}}$ of 0.025, $E_{a,nuc}$(T → M) and $E_{a,nuc}$(T → PO) decrease by 0.89 eV and 0.85 eV in $Hf_{0.5}Zr_{0.5}O_2$, and 0.79 eV and 0.22 eV in ZrO_2, respectively. Under compressive $\varepsilon_{\{111\}}$, on

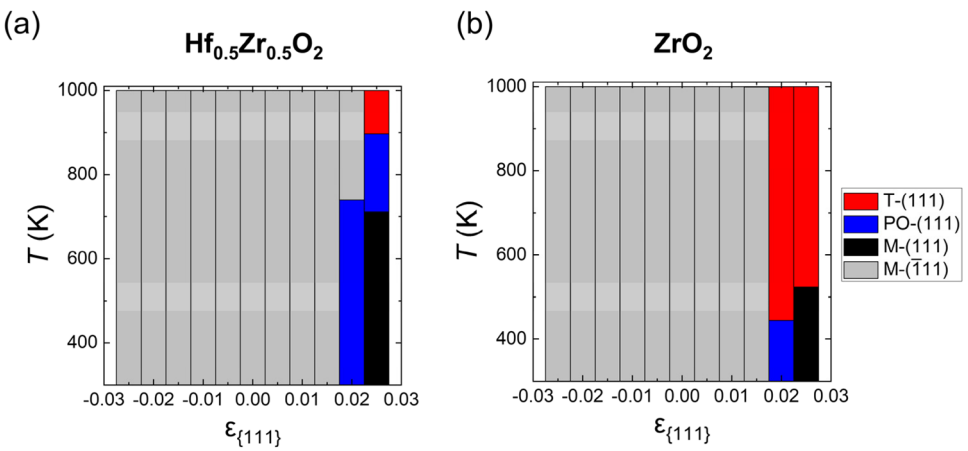

Fig. 3 Ground state depending on $\varepsilon_{\{111\}}$ and T of (a) $Hf_{0.5}Zr_{0.5}O_2$ and (b) ZrO_2. The red, blue, black, and gray colors indicate that the T-(111), PO-(111), M-(111), and M-($\bar{1}$11) oriented grains have the lowest $F_{i,grain}$ at the given $\varepsilon_{\{111\}}$ and temperature, respectively.

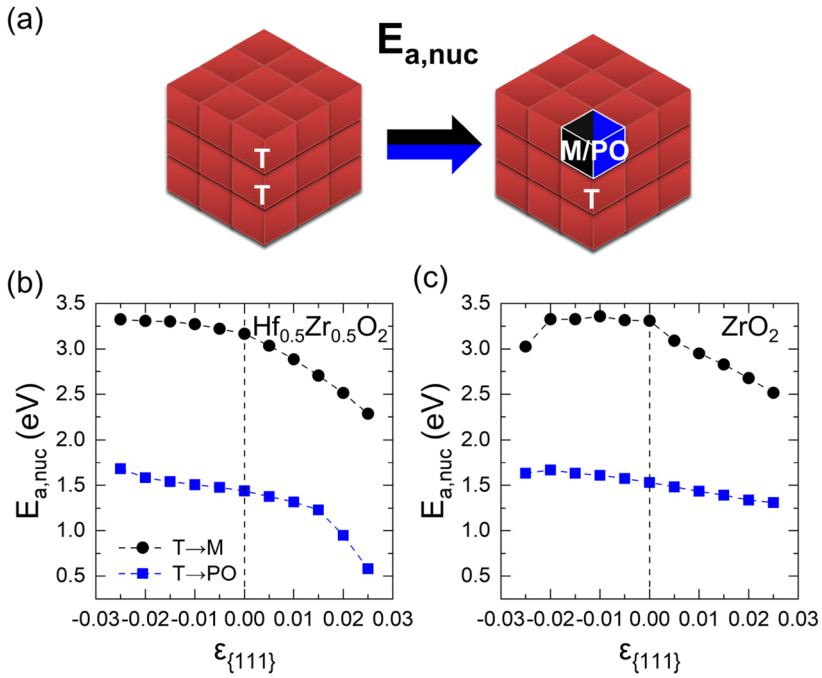

Fig. 4 (a) Schematics of $E_{a,nuc}$ from the T- to M or PO-phase. The $\varepsilon_{\{111\}}$-dependent $E_{a,nuc}$(T → M) and $E_{a,nuc}$(T → PO) of (b) $Hf_{0.5}Zr_{0.5}O_2$ and (c) ZrO_2.

the other hand, $E_{a,nuc}$ increases only marginally. The variations in $E_{a,nuc}$ with $\varepsilon_{\{111\}}$ could be related to the unit cell volume change. As presented in Fig. S8,† the unit cell volumes of polymorphs in $Hf_{0.5}Zr_{0.5}O_2$ and ZrO_2 increase (decrease) as $\varepsilon_{\{111\}}$ increases (decreases). Since the equilibrium unit cell volumes of the M- and PO-phases are larger than that of the T-phase, the PO- and M-phases can be more stabilized under tensile $\varepsilon_{\{111\}}$. Thus, the tensile $\varepsilon_{\{111\}}$ results in smaller $E_{a,nuc}$ values.

In-plane strain effects on the phase fraction

Amorphous HZO is generally formed in the ALD process, and subsequent heat treatment is required for crystallization. The crystallized fraction of the i-phase from amorphous ($C_{i,crystn}$) could be calculated from its crystallization barrier according to our previous study,[17] and the results are described in Fig. S9.† In $Hf_{0.5}Zr_{0.5}O_2$, $C_{T,crystn}$ gradually increased from 0.86 at 700 K to 0.99 at 1000 K, and the $C_{M,crystn}$ was calculated to be 1 − $C_{T,crystn}$. The PO-phase fraction, $C_{PO,crystn}$, is negligible due to its high crystallization barrier. In ZrO_2, on the other hand, $C_{T,crystn}$ is ~1.00 across the entire temperature range. The details on the crystallization process are reported elsewhere,[17] and are also summarized in SM. However, the effect of strain on the crystallization process could not be considered because applying strain in an amorphous structure was challenging. In addition, $C_{M,crystn}$ was assumed to remain unchanged in the subsequent heat treatment and cooling step after crystallization in this study because the M-phase generally forms the ground state, even if a slight in-plane strain is applied. Besides, the T-phase is the primary phase formed from amorphous $Hf_{0.5}Zr_{0.5}O_2$ and ZrO_2. Due to the metastability of the T-phase, transitions from the T-phase to other phases occur during the subsequent process. Therefore, this section focuses on transitions from the T- to M- and PO-phases during annealing and cooling, taking into account the effects of $\varepsilon_{\{111\}}$ on both the thermodynamic ($F_{i,grain}$) and kinetic ($E_{a,nuc}$) terms.

Due to the lower $E_{a,nuc}$(T → PO) than $E_{a,nuc}$(T → M), the phase transition from the T- to PO-phases is faster than that from the T- to M-phases. However, in this study, the fraction transitioned from the T- to M-phases ($C_{T\to M}$) was calculated prior to that from the T- to PO phases ($C_{T\to PO}$) because the high $E_{a,nuc}$(T → M) allows for the M-phase formation only during annealing, not during cooling. Nonetheless, the calculation sequence does not significantly affect the overall phase fractions because the transition from the T- to PO-phases is suppressed at high annealing temperatures due to the higher stability of the T-phase than the PO-phase. At low annealing temperatures, the transition to M-phase is small from both T- and PO-phases due to low thermal energy. Therefore, the total phase fractions are negligibly affected even if the PO-phase forms before the M-phase.

The equilibrium fraction of the M-phase transformed from the T-phase ($C_{T\to M}^{Boltzmann}$) is described by the Boltzmann distribution of $F_{i,grain}$.

$$C_{T\to M}^{Boltzmann}(T) = C_{T,crystn}\frac{\exp\left(-\frac{F_{M,grain}}{k_BT}\right)}{\exp\left(-\frac{F_{M,grain}}{k_BT}\right)+\exp\left(-\frac{F_{PO,grain}}{k_BT}\right)+\exp\left(-\frac{F_{T,grain}}{k_BT}\right)} \quad (3)$$

This equation is valid only when the thermal energy is sufficient to overcome the $E_{a,nuc}$(T → M), which is generally

not the case at moderate annealing temperatures (~700K), rendering the kinetically formed fraction smaller than the $C_{T\to M}^{Boltzmann}$. To address the kinetic effect, the kinetically limited fraction of the M-phase transformed from the T-phase ($C_{T\to M}^{JMA}$) was calculated based on the Johnson–Mehl–Avrami (JMA) equation:

$$C_{T\to M}^{JMA}(T) = C_{T,crystn}[1 - \exp(-(k_{T\to M}(T)\cdot t_{annealing})^n)], \quad (4)$$

where $t_{annealing}$ and n denote the annealing time and Avrami exponent with values of 30 s and 0.25, estimated from a previous experiment.[39] $k_{T\to i}(T)$ is the temperature-dependent rate constant of transition from the T- to i-phase, given as eqn (5):

$$k_{T\to i}(T) = \nu_0 \exp\left(\frac{-E_{a,nuc}(T\to i)}{k_B T}\right) \quad (5)$$

where ν_0 is the atomic vibration frequency, assumed to be 10^{13} s^{-1}. As a result, $C_{T\to M}$ is determined by the smaller factor between the thermodynamic and kinetic effects, represented by eqn (3) and eqn (4), respectively. Therefore, the $T_{annealing}$-dependent $C_{T\to M}$ is calculated by using eqn (6):

$$C_{T\to M} = \begin{cases} C_{T\to M}^{JMA}(T_{annealing}) & (T_{annealing} < T_{equil,M}) \quad (6\text{-}1) \\ C_{T\to M}^{Boltzmann}(T_{equil,M}) & (T_{annealing} \geq T_{equil,M}) \quad (6\text{-}2) \end{cases}.$$

In eqn (6), the equilibrium temperature of the M-phase ($T_{equil,M}$) is the temperature where $C_{T\to M}^{Boltzmann}(T)$ and $C_{T\to M}^{JMA}(T)$ are equal. Thus, $C_{T\to M}$ is determined as $C_{T\to M}^{Boltzmann}(T_{equil,M})$ or $C_{T\to M}^{JMA}(T_{annealing})$ if the heat treatment is conducted at $T_{annealing}$ higher or lower than $T_{equil,M}$. Fig. 5(a) shows the variations in $C_{T\to M}^{Boltzmann}$ and $C_{T\to M}^{JMA}$ of $Hf_{0.5}Zr_{0.5}O_2$ as a function of $T_{annealing}$ when $\varepsilon_{\{111\}} = 0.00$. Below 1160 K, $C_{T\to M}^{JMA}$ is lower than $C_{T\to M}^{Boltzmann}$, indicating that thermal energy is insufficient to achieve thermal equilibrium. Hence, the $C_{T\to M}$ is determined by $C_{T\to M}^{JMA}$ following eqn (6-1). Above 1160 K, in contrast, $C_{T\to M}^{JMA}$ is greater than $C_{T\to M}^{Boltzmann}$, representing that thermal energy is enough to establish thermal equilibrium. Therefore, $C_{T\to M}$ is saturated to $C_{T\to M}^{Boltzmann}(T_{equil,M})$ following eqn (6-2).

Meanwhile, the PO-phase transition from the T-phase ($C_{T\to PO}$) is also determined similarly to $C_{T\to M}$. Due to the much lower $E_{a,nuc}(T \to PO)$ than $E_{a,nuc}(T \to M)$ for all $\varepsilon_{\{111\}}$ shown in Fig. 4, the transition from the T- to the PO-phases is expected to occur during both annealing and cooling. This fact manifests that thermal equilibrium between the T- and PO-phases is maintained at a specific cooling temperature. In other words, the equilibrium temperature of the PO-phase ($T_{equil,PO}$), where $C_{T\to PO}^{Boltzmann}(T)$ and $C_{T\to PO}^{JMA}(T)$ are equal, is lower than the usual annealing temperatures. After annealing, the equilibrium phase fraction of the PO-phase was also calculated by the Boltzmann distribution of $F_{i,grain}$ as shown in eqn (7).

$$C_{T\to PO}^{Boltzmann}(T) = (C_{T,crystn} - C_{T\to M}) \times \frac{\exp\left(-\frac{F_{PO,grain}}{k_B T}\right)}{\exp\left(-\frac{F_{PO,grain}}{k_B T}\right) + \exp\left(-\frac{F_{T,grain}}{k_B T}\right)} \quad (7)$$

The M-phase formed during annealing was assumed not to participate in the cooling process due to the high $E_{a,nuc}(T \to M)$. Thus, the $C_{T\to PO}$ was determined from the T-phase remaining in the annealing process ($C_{T,crystn}$–$C_{T\to M}$). The kinetically limited fraction of the PO-phase transformed from the T-phase ($C_{T\to PO}^{JMA}$) during cooling was calculated based on the JMA equation shown in eqn (8).

$$C_{T\to PO}^{JMA}(T) = (C_{T,crystn} - C_{T\to M})[1 - \exp(-(k_{T\to PO}(T)\cdot t_{cooling})^n)] \quad (8)$$

Eqn (8) is similar to eqn (4), but a cooling time ($t_{cooling}$) of 0.5 s (according to the moderate cooling rate of 2 K s^{-1})[40] was used instead of $t_{annealing}$, meaning that $C_{T\to PO}^{JMA}$ was calculated for $Hf_{0.5}Zr_{0.5}O_2$ annealed at each T for 0.5 s.

Fig. 5(b) shows the $C_{T\to PO}^{Boltzmann}$ and $C_{T\to PO}^{JMA}$ of $Hf_{0.5}Zr_{0.5}O_2$ at $\varepsilon_{\{111\}} = 0.00$ when annealed at 700 K and then cooled to room temperature. $T_{equil,PO}$ was determined to be 570 K, and, hence, the thermal equilibrium is achieved above 570 K and the PO-phase forms with a fraction of $C_{T\to PO}^{Boltzmann}$. Below 570 K,

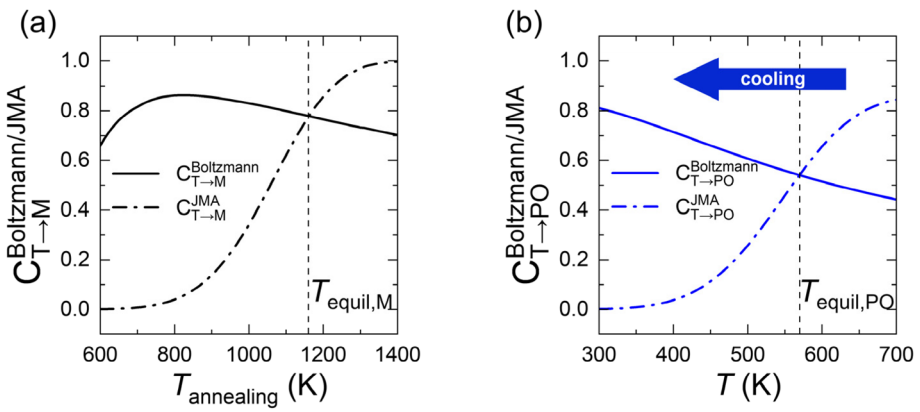

Fig. 5 (a) $T_{annealing}$-dependent $C_{T\to M}^{Boltzmann}$ and $C_{T\to M}^{JMA}$ in $Hf_{0.5}Zr_{0.5}O_2$ at $\varepsilon_{\{111\}} = 0.00$. (b) T-dependent $C_{T\to PO}^{Boltzmann}$ and $C_{T\to PO}^{JMA}$ when annealed at 700 K and cooled down to 300 K in $Hf_{0.5}Zr_{0.5}O_2$ at $\varepsilon_{\{111\}} = 0.00$. The solid and dash-dotted lines represent the phase fractions calculated by the Boltzmann distribution and the Johnson–Mehl–Avrami equation, respectively. The vertical dashed lines in (a) and (b) present $T_{equil,M}$ and $T_{equil,PO}$, respectively.

however, the PO-phase is no longer formed due to insufficient thermal energy to overcome the kinetic energy barrier. Therefore, the $C_{T\rightarrow PO}$ in the cooling process converges to $C_{T\rightarrow PO}^{Boltzmann}(T_{equil,PO})$. Fig. S10† shows the $\varepsilon_{\{111\}}$-dependent $T_{equil,M}$ and $T_{equil,PO}$ in $Hf_{0.5}Zr_{0.5}O_2$ and ZrO_2, respectively. Overall, $T_{equil,M}$ exceeds the normal $T_{annealing}$ of polycrystalline films (= 700–800 K), but $T_{equil,PO}$ is much lower than $T_{annealing}$ regardless of $\varepsilon_{\{111\}}$. These facts indicate that the M-phase formation is kinetically suppressed. At the same time, the thermodynamic driving force and facile kinetic route at the normal crystallization, annealing, and cooling temperatures support the PO-phase formation.

Fig. 6 shows the overall calculation procedure for the sequential crystallization, annealing, and cooling processes. The total fractions of the M-, PO-, and T-phases were calculated as $C_M = C_{M,crystn} + C_{T\rightarrow M}$, $C_{PO} = C_{T\rightarrow PO}$, and $C_T = 1 - C_M - C_{PO}$, respectively.

Fig. 7(a) and (b) show the effects of $\varepsilon_{\{111\}}$ on the phase fractions formed after the cooling when the $Hf_{0.5}Zr_{0.5}O_2$ film was crystallized at $T_{annealing}$ of 700 K and 1000 K with a d_T of 10 nm. The red, blue, and gray colors represent the fractions of the T-(111), PO-(111), and M-{111} grains, respectively. The hatch and cross patterns in the PO- and M-phases indicate that the formation of the corresponding phases is governed by thermodynamic factors (*i.e.*, controlled by the Boltzmann distribution) and kinetic factors (*i.e.*, controlled by the JMA equation), respectively. As discussed above, $C_{T\rightarrow PO}$ is solely determined by the thermodynamic factors; all the $C_{T\rightarrow PO}$ regions have the hatch pattern. In contrast, $C_{T\rightarrow M}$ is determined by either thermodynamic or kinetic factors, so it has a hatch or cross pattern, depending on the detailed formation conditions.

At $T_{annealing}$ = 700 K shown in Fig. 7(a), the $C_{T\rightarrow PO}$ has a maximum value at $\varepsilon_{\{111\}}$ = 0.02 and diminishes with decreasing $\varepsilon_{\{111\}}$ due to the increase of $F_{PO,grain}$. Meanwhile, the PO-(111) is thermodynamically stable at $\varepsilon_{\{111\}}$ = 0.025 and T = 700 K in Fig. 3(a), but the $C_{T\rightarrow PO}$ at $\varepsilon_{\{111\}}$ = 0.025 is lower than those at $\varepsilon_{\{111\}}$ = 0.01 and 0.015 where the PO-phase is not the ground state. This behavior is due to the abrupt increase of $C_{T\rightarrow M}$ along with $\varepsilon_{\{111\}}$, caused by a significant decrease in $E_{a,nuc}(T \rightarrow M)$ shown in Fig. 4(b).

At $T_{annealing}$ = 1000 K shown in Fig. 7(b), on the other hand, the $C_{M,crystn}$ is negligibly low irrespective of $\varepsilon_{\{111\}}$. However, over the entire $\varepsilon_{\{111\}}$ range, the $C_{T\rightarrow M}$ significantly increases compared to that shown in Fig. 7(a), indicating that a very high annealing temperature is undesirable. Interestingly, $C_{T\rightarrow M}$ increases with increasing $\varepsilon_{\{111\}}$ as long as the kinetic factor governs the M-phase formation. In contrast, it diminishes with increasing $\varepsilon_{\{111\}}$ once the M-phase formation is dominated by the thermodynamic factor, as represented by the hatch pattern. The optimal $\varepsilon_{\{111\}}$ to increase the $C_{T\rightarrow PO}$ depends on $T_{annealing}$. As the $T_{annealing}$ increases, the $C_{T\rightarrow PO}$ decreases due to the overall increment of $C_{T\rightarrow M}$. Therefore, to maximize C_{PO} while suppressing C_M, annealing at moderate temperatures (~700 K) and tensile $\varepsilon_{\{111\}}$ is suitable, which is consistent with the experimental results of polycrystalline $Hf_{0.5}Zr_{0.5}O_2$ annealed at different temperatures and under different in-plane strain conditions.[7,8,32,35]

Fig. 7(c) shows the phase fractions in the extreme case when sufficient thermal energy is supplied by annealing at elevated temperatures (*i.e.*, $T_{annealing}$ is higher than $T_{equil,M}$ in all $\varepsilon_{\{111\}}$), where all the $C_{T\rightarrow M}$ is saturated to $C_{T\rightarrow M}^{Boltzmann}(T_{equil,\ M})$, represented by the hatch pattern across the entire gray bars. The $C_{T\rightarrow PO}$ increases with increasing $\varepsilon_{\{111\}}$, indicating that the tensile strain state is favored over the compressive one even under these extreme temperature conditions. Also, $C_{T\rightarrow PO}$ at $\varepsilon_{\{111\}}$ of 0.02–0.025 is higher than $C_{T\rightarrow M}$ because the difference between $F_{PO,grain}$ and $F_{M,grain}$ decreases in this $\varepsilon_{\{111\}}$ range. These calculation results explain the enhanced ferroelectricity in epitaxial $Hf_{0.5}Zr_{0.5}O_2$ films under in-plane tensile strain and the reduction of ferroelectricity due to the increase in the M-phase under in-plane compressive strain in thin films deposited at temperatures above 1000 K.[9,12,41]

Fig. 8 shows similar calculation results for ZrO_2 as Fig. 7. The tendency of the phase fractions depending on $\varepsilon_{\{111\}}$ is similar to that of $Hf_{0.5}Zr_{0.5}O_2$. In ZrO_2, however, the M-phase

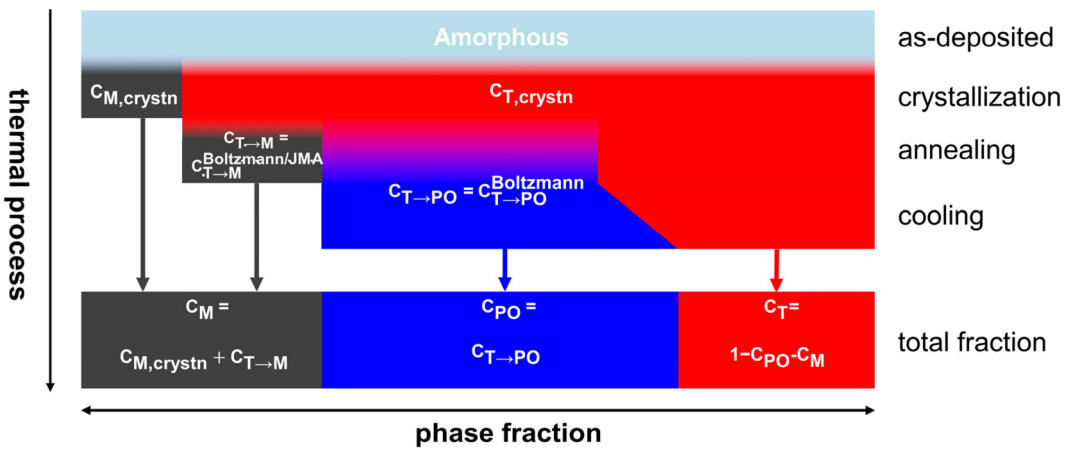

Fig. 6 Calculation procedure of the phase transition and phase fractions in the whole thermal processes in HZO.

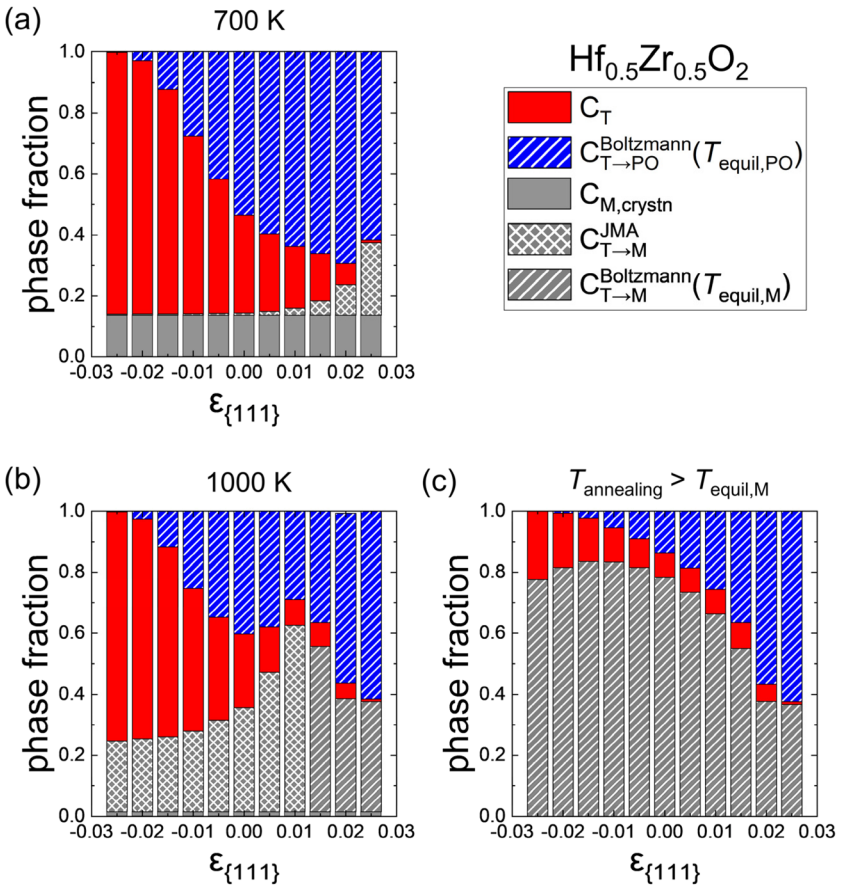

Fig. 7 Phase fractions formed after the whole thermal processes in $Hf_{0.5}Zr_{0.5}O_2$ as a function of $\varepsilon_{\{111\}}$ at $T_{annealing}$ of (a) 700 K and (b) 1000 K. (c) Phase fractions in the extreme case when $T_{annealing}$ is higher than $T_{equil,M}$. The red, blue, and gray colors represent the T-(111), PO-(111), and M-{111} grains, respectively. The hatch and cross patterns in $C_{T\rightarrow M}$ and $C_{T\rightarrow PO}$ indicate the phase formation from the T-phase that is governed by thermodynamics (Boltzmann distribution) and kinetics (JMA equation), respectively.

formation is more suppressed, and the T-phase is the primary phase rather than the PO-phase. These results are due to lower $C_{M,crystn}$ (= ~0), lower $F_{T,grain}$, and higher $E_{a,nuc}(T \rightarrow M)$ in ZrO_2 compared to $Hf_{0.5}Zr_{0.5}O_2$. Nevertheless, $C_{T\rightarrow PO}$ increases with tensile $\varepsilon_{\{111\}}$, suggesting an increase of (field-induced) ferroelectricity through tensile $\varepsilon_{\{111\}}$ engineering.

In-plane strain effects on the ferroelectric polarization

Finally, the effects of $\varepsilon_{\{111\}}$ on the theoretical polarizations of $Hf_{0.5}Zr_{0.5}O_2$ and ZrO_2 were calculated. Fig. 9(a) depicts the two polarization switching pathways of the shift-inside (SI) and the shift across (SA) in the PO-phase. Due to the presence of the two switching paths, $Hf_{0.5}Zr_{0.5}O_2$ exhibits two P_s of 58 and 66 μC cm^{-2} in the [001] orientation at $\varepsilon_{\{111\}}$ = 0.00 for the SI and SA pathways, respectively. Early studies often reported a lower ferroelectric switching barrier for the SI pathway when calculating the switching barriers in the 1 × 1 × 1 PO-phase unit cell.[42,43] However, recent studies demonstrated that the SA pathway is more adjustable when computing in the N × 1 × 1 PO-phase supercell.[44,45] Thus, this study examines both switching pathways. Fig. 9(b) and (c) show the $\varepsilon_{\{111\}}$-dependent P_s along the [001] orientation in $Hf_{0.5}Zr_{0.5}O_2$ and ZrO_2. The P_s of the SI pathway increases with compressive $\varepsilon_{\{111\}}$, while the P_s of the SA pathway increases with tensile $\varepsilon_{\{111\}}$.

For P_r calculation, the [111] orientation is assumed as an out-of-plane direction. Hence, the polarization along the [111] direction was considered as $P_s/\sqrt{3}$. In addition, the C_{PO} was also considered for calculating the theoretical P_r because only the PO-phase contributes to the ferroelectric polarization. As a result, theoretical P_r was calculated as $C_{PO} \times P_s/\sqrt{3}$. Fig. 9(d) shows the P_r of $Hf_{0.5}Zr_{0.5}O_2$ depending on $\varepsilon_{\{111\}}$ when the $T_{annealing}$ is 700 K. The P_r of $Hf_{0.5}Zr_{0.5}O_2$ at $\varepsilon_{\{111\}}$ = 0.00–0.025 ranges from 18–21 μC cm^{-2} by the SI pathway, while 20–28 μC cm^{-2} by the SA pathway, consistent with the experimental P_r values (10–30 μC cm^{-2}) in $Hf_{0.5}Zr_{0.5}O_2$.[2,3] Compared to $\varepsilon_{\{111\}}$ = 0.00, the P_r of $Hf_{0.5}Zr_{0.5}O_2$ increases *via* tensile $\varepsilon_{\{111\}}$ by 19% and 34% by the SI and SA pathways, respectively. The more pronounced increase of P_r in the SA pathway is attributed to the increase of P_s in the SA pathway under tensile $\varepsilon_{\{111\}}$. On the other hand, P_r in ZrO_2 was lower than that in $Hf_{0.5}Zr_{0.5}O_2$ for all the $\varepsilon_{\{111\}}$ ranges in Fig. 9(e). However, its increase ratios were 84% (SI pathway) and 106% (SA pathway), much higher than those in $Hf_{0.5}Zr_{0.5}O_2$. Therefore, in-plane tensile strain engineering is suitable for applications requiring high P_r in

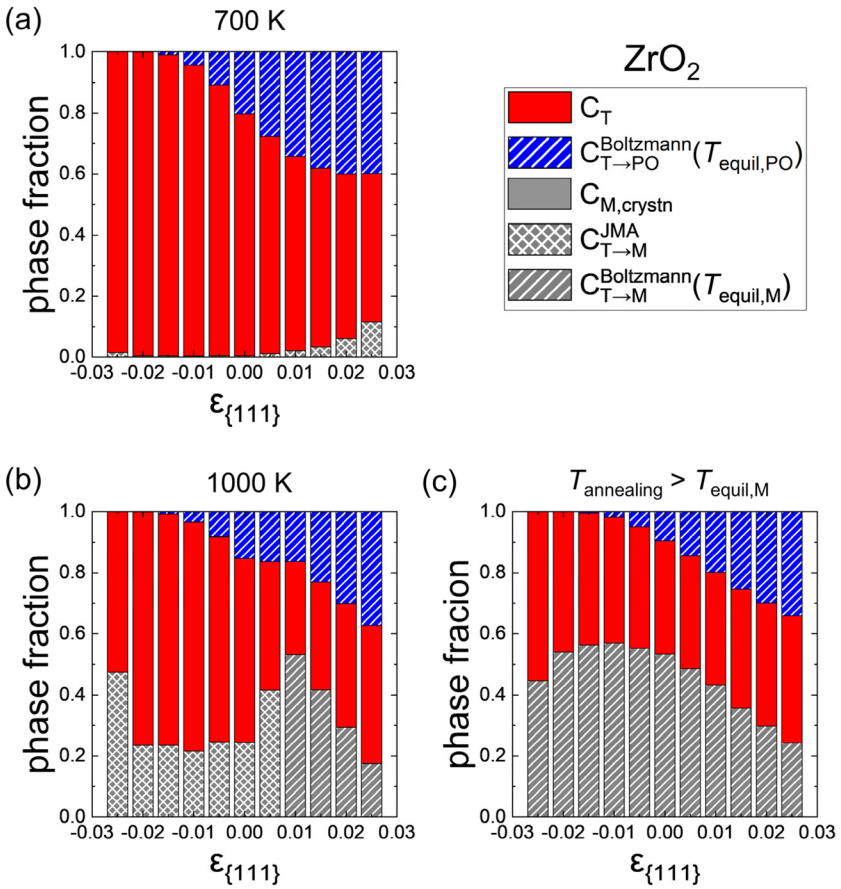

Fig. 8 Phase fractions formed after the whole thermal processes in ZrO_2 as a function of $\varepsilon_{\{111\}}$ at $T_{annealing}$ of (a) 700 K and (b) 1000 K. (c) Phase fractions in the extreme case when $T_{annealing}$ is higher than $T_{equil,M}$. The red, blue, and gray colors represent the T-(111), PO-(111), and M-{111} grains, respectively. The hatch and cross patterns in $C_{T\rightarrow M}$ and $C_{T\rightarrow PO}$ indicate the phase formation from the T-phase that is governed by thermodynamics (Boltzmann distribution) and kinetics (JMA equation), respectively.

$Hf_{0.5}Zr_{0.5}O_2$ and ZrO_2, irrespective of the switching pathways. The in-plane tensile strain can be experimentally realized by various ways, such as the thermal expansion coefficient mismatch between the film and electrode,[8] lattice parameter mismatch between the film and substrate,[9] and the growth mode control,[29] which will increase the PO-phase fraction.

Conclusion

The in-plane strain-dependent phase fractions were predicted using density functional theory calculations to understand the enhanced ferroelectricity in tensile-strained $Hf_{0.5}Zr_{0.5}O_2$ and ZrO_2 thin films in the experiment. The thermodynamic free energy and kinetic activation barrier for the phase transition from the tetragonal (T-) phase to monoclinic (M-) or polar orthorhombic (PO-) phases were calculated as a function of in-plane strain. They were employed for the Boltzmann distribution and the Johnson–Mehl–Avrami (JMA) equation for the phase fraction calculations. This methodology enabled the computation of quantitative phase fractions as a function of in-plane strain with the ⟨111⟩ orientation ($\varepsilon_{\{111\}}$) and annealing temperature. The JMA equation (kinetic factors) primarily determined the M-phase fraction at low temperatures due to the high activation barrier for the transition from the T- to M-phases. The kinetically formed M-phase fraction increases as temperature increases due to the increment of thermal energy. If temperatures are sufficiently high to overcome this activation barrier, the M-phase fraction converges to the value obtained from the Boltzmann distribution (thermodynamic factors).

On the other hand, the activation barrier from the T- to PO-phases is relatively low, making the thermodynamic factors mainly control the PO-phase formation. The PO-phase fraction increases in the tensile $\varepsilon_{\{111\}}$ region, where the PO-phase has relatively low free energy. Conversely, the T-phase is preferred in the compressive $\varepsilon_{\{111\}}$ region, where the PO-phase has high free energy. Therefore, heat treatment at moderate temperatures at 700–800 K and applying in-plane tensile $\varepsilon_{\{111\}}$ are appropriate for suppressing the M-phase formation and enhancing the PO-phase formation. These calculation results are consistent with general experimental observations on the enhanced ferroelectricity of polycrystalline $Hf_{0.5}Zr_{0.5}O_2$ films under in-plane tensile strain annealed at approximately 700–800 K. In addition, the abundant PO-phase fraction under

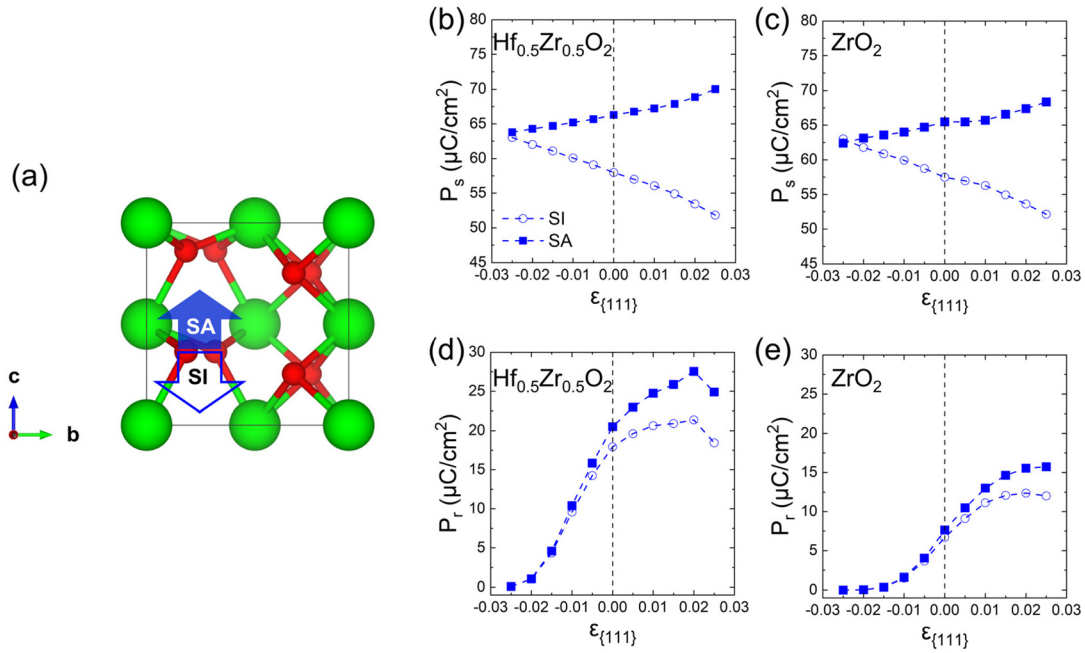

Fig. 9 (a) Switching pathways of shift-inside (SI) and shift-across (SA) in the PO-phase. (b and c) P_s along the [001] orientation of SI and SA pathways depending on $\varepsilon_{\{111\}}$ in (b) $Hf_{0.5}Zr_{0.5}O_2$ and (c) ZrO_2. (d and e) P_r along the [111] orientation of SI and SA pathways depending on $\varepsilon_{\{111\}}$ in (d) $Hf_{0.5}Zr_{0.5}O_2$ and (e) ZrO_2 when $T_{annealing}$ = 700 K.

a tensile $\varepsilon_{\{111\}}$ of 0.02–0.025 in the higher temperature region (>1000 K) is consistent with the enhanced ferroelectricity in the epitaxial $Hf_{0.5}Zr_{0.5}O_2$ film when deposited at high temperatures. The polarization values were quantitatively calculated by taking into account the PO-phase fraction. The remanent polarization increases by 34% in $Hf_{0.5}Zr_{0.5}O_2$ and 106% in ZrO_2 under tensile strain. This study overcomes the gap between theoretical predictions and experimental results by elucidating that in-plane tensile $\varepsilon_{\{111\}}$ is suitable for increasing the PO-phase fraction and enhancing ferroelectricity. Furthermore, the strain engineering proposed in this study is expected to also contribute to optimizing other electrical properties, such as high-*k* applications.

Author contributions

Kun Hee Ye: formal analysis, investigation, methodology, and writing – original draft; Taeyoung Jeong: formal analysis and writing – review & editing; Seungjae Yoon: formal analysis and writing – review & editing; Dohyun Kim: formal analysis and writing – review & editing; Cheol Seong Hwang: supervision and writing – review & editing; and Jung-Hae Choi: conceptualization, funding acquisition, project administration, supervision, and writing – review & editing.

Data availability

The data that support the findings of this study are available within this article and its ESI.†

Conflicts of interest

The authors declare that they have no known competing financial interests or personal relationships that could have appeared to influence the work reported in this paper.

Acknowledgements

J.-H.C. was supported by the National Research Foundation of Korea (NRF) grant funded by MSIT [Next Generation Intelligence Semiconductor Foundation 2022M3F3A2A01076569] and by the Institutional Research Program of Korea Institute of Science and Technology (KIST) [2E33223]. C.S.H. was supported by the Technology Innovation Program [20017224, Development of a new ALD system for the next-generation mass-production memory devices] funded by the Ministry of Trade Industry & Energy [MOTIE, Korea]. The authors would also like to acknowledge the support from the KISTI Supercomputing Center through a Strategic Support Program for Supercomputing Application Research [KSC-2022-CRE-0378 and KSC-2023-CRE-0410].

References

1 J. P. B. Silva, R. Alcala, U. E. Avci, N. Barrett, L. Bégon-Lours, M. Borg, S. Byun, S. C. Chang, S. W. Cheong, D. H. Choe, J. Coignus, V. Deshpande, A. Dimoulas, C. Dubourdieu, I. Fina, H. Funakubo, L. Grenouillet, A. Gruverman, J. Heo, M. Hoffmann, H. A. Hsain, F. T. Huang, C. S. Hwang, J. Íñiguez, J. L. Jones,

I. V. Karpov, A. Kersch, T. Kwon, S. Lancaster, M. Lederer, Y. Lee, P. D. Lomenzo, L. W. Martin, S. Martin, S. Migita, T. Mikolajick, B. Noheda, M. H. Park, K. M. Rabe, S. Salahuddin, F. Sánchez, K. Seidel, T. Shimizu, T. Shiraishi, S. Slesazeck, A. Toriumi, H. Uchida, B. Vilquin, X. Xu, K. H. Ye and U. Schroeder, *APL Mater.*, 2023, **11**, 089201.

2 U. Schroeder, M. H. Park, T. Mikolajick and C. S. Hwang, *Nat. Rev. Mater.*, 2022, **7**, 653–669.

3 M. H. Park, Y. H. Lee, H. J. Kim, Y. J. Kim, T. Moon, K. D. Kim, J. Müller, A. Kersch, U. Schroeder, T. Mikolajick and C. S. Hwang, *Adv. Mater.*, 2015, **27**, 1811–1831.

4 J. Müller, T. S. Böscke, U. Schröder, S. Mueller, D. Bräuhaus, U. Böttger, L. Frey and T. Mikolajick, *Nano Lett.*, 2012, **12**, 4318–4323.

5 S. D. Hyun, H. W. Park, M. H. Park, Y. H. Lee, Y. B. Lee, B. Y. Kim, H. H. Kim, B. S. Kim and C. S. Hwang, *Adv. Electron. Mater.*, 2020, **6**, 2000631.

6 M. Jung, V. Gaddam and S. Jeon, *Nano Converg.*, 2022, **9**, 44.

7 S. J. Kim, D. Narayan, J. G. Lee, J. Mohan, J. S. Lee, J. Lee, H. S. Kim, Y. C. Byun, A. T. Lucero, C. D. Young, S. R. Summerfelt, T. San, L. Colombo and J. Kim, *Appl. Phys. Lett.*, 2017, **111**, 242901.

8 Y. Goh, J. Hwang, Y. Lee, M. Kim and S. Jeon, *Appl. Phys. Lett.*, 2020, **117**, 242901.

9 S. Estandía, N. Dix, J. Gazquez, I. Fina, J. Lyu, M. F. Chisholm, J. Fontcuberta and F. Sánchez, *ACS Appl. Electron. Mater.*, 2019, **1**, 1449.

10 R. Batra, H. D. Tran and R. Ramprasad, *Appl. Phys. Lett.*, 2016, **108**, 172902.

11 R. Materlik, C. Kunneth and A. Kersch, *J. Appl. Phys.*, 2015, **117**, 134109.

12 K. Liu, F. Jin, X. Zhang, K. Liu, Z. Zhang, E. Hua, J. Zhang, H. Ye, G. Gao, C. Ma, L. Wang and W. Wu, *Adv. Funct. Mater.*, 2023, **33**, 2209925.

13 J. F. Ihlefeld, T. Peters, S. T. Jaszewski, T. Mimura, B. L. Aronson and S. Trolier-McKinstry, *Appl. Phys. Lett.*, 2023, **123**, 082901.

14 Y. Zhang, Q. Yang, L. Tao, E. Y. Tsymbal and V. Alexandrov, *Phys. Rev. Appl.*, 2020, **14**, 014068.

15 S. Liu and B. M. Hanrahan, *Phys. Rev. Mater.*, 2019, **3**, 054404.

16 K. Chae, J. Hwang, E. Chagarov, A. Kummel and K. Cho, *J. Appl. Phys.*, 2020, **128**, 054101.

17 K. H. Ye, I. W. Yeu, G. Han, T. Jeong, S. Yoon, D. Kim, C. S. Hwang and J. H. Choi, *Appl. Phys. Rev.*, 2023, **10**, 031419.

18 G. Kresse and J. Furthmüller, *Phys. Rev. B: Condens. Matter Mater. Phys.*, 1996, **54**, 11169.

19 G. Kresse and J. Furthmüller, *Comput. Mater. Sci.*, 1996, **6**, 15–50.

20 D. M. Ceperley and B. J. Alder, *Phys. Rev. Lett.*, 1980, **45**, 566.

21 J. P. Perdew and A. Zunger, *Phys. Rev. B: Condens. Matter Mater. Phys.*, 1981, **23**, 5048.

22 G. Kresse and D. Joubert, *Phys. Rev. B: Condens. Matter Mater. Phys.*, 1999, **59**, 1758.

23 P. E. Blöchl, *Phys. Rev. B: Condens. Matter Mater. Phys.*, 1994, **50**, 17953.

24 A. Togo and I. Tanaka, *Scr. Mater.*, 2015, **108**, 1.

25 R. D. King-Smith and D. Vanderbilt, *Phys. Rev. B: Condens. Matter Mater. Phys.*, 1993, **47**, 1651.

26 N. A. Spaldin, *J. Solid State Chem.*, 2012, **195**, 2–10.

27 A. Christensen and E. A. Carter, *Phys. Rev. B: Condens. Matter Mater. Phys.*, 1998, **58**, 8050.

28 M. H. Park, Y. H. Lee, H. J. Kim, Y. J. Kim, T. Moon, K. Do Kim, S. D. Hyun, T. Mikolajick, U. Schroeder and C. S. Hwang, *Nanoscale*, 2018, **10**, 716–725.

29 M. H. Park, H. J. Kim, Y. J. Kim, T. Moon and C. S. Hwang, *Appl. Phys. Lett.*, 2014, **104**, 072901.

30 C. Verdi, F. Karsai, P. Liu, R. Jinnouchi and G. Kresse, *npj Comput. Mater.*, 2021, **7**, 156.

31 M. H. Park, Y. H. Lee, H. J. Kim, T. Schenk, W. Lee, K. Do Kim, F. P. G. Fengler, T. Mikolajick, U. Schroeder and C. S. Hwang, *Nanoscale*, 2017, **9**, 9973–9986.

32 J. Wu, F. Mo, T. Saraya, T. Hiramoto and M. Kobayashi, *Appl. Phys. Lett.*, 2020, **117**, 252904.

33 M. H. Park, Y. H. Lee and C. S. Hwang, *Nanoscale*, 2019, **11**, 19477–19487.

34 D. A. Porter, K. E. Easterling and M. Y. Sherif, *Phase Transformations in Metals and Alloys*, CRC Press, USA, 3rd edn, 2009.

35 M. H. Park, H. J. Kim, Y. J. Kim, W. Lee, T. Moon and C. S. Hwang, *Appl. Phys. Lett.*, 2013, **102**, 242905.

36 S. Dutta, P. Buragohain, S. Glinsek, C. Richter, H. Aramberri, H. Lu, U. Schroeder, E. Defay, A. Gruverman and J. Íñiguez, *Nat. Commun.*, 2021, **12**, 7301.

37 R. M. P. Pereira, M. C. Istrate, F. G. Figueiras, V. Lenzi, B. M. Silva, M. Benamara, K. N. Romanyuk, C. Ghica, B. G. Almeida, L. Marques, M. Pereira and J. P. B. Silva, *Mater. Sci. Semicond. Process.*, 2024, **172**, 108102.

38 R. Ganser, S. Bongarz, A. Von Mach, L. Azevedo Antunes and A. Kersch, *Phys. Rev. Appl.*, 2022, **18**, 054066.

39 Y. H. Lee, S. D. Hyun, H. J. Kim, J. S. Kim, C. Yoo, T. Moon, K. Do Kim, H. W. Park, Y. Bin Lee, B. S. Kim, J. Roh, M. H. Park and C. S. Hwang, *Adv. Electron. Mater.*, 2019, **5**, 1800436.

40 S. S. Fields, T. Cai, S. T. Jaszewski, A. Salanova, T. Mimura, H. H. Heinrich, M. D. Henry, K. P. Kelley, B. W. Sheldon and J. F. Ihlefeld, *Adv. Electron. Mater.*, 2022, **8**, 2200601.

41 T. Song, V. Lenzi, J. P. B. Silva, L. Marques, I. Fina and F. Sánchez, *Appl. Phys. Rev.*, 2023, **10**, 041415.

42 W. Wei, G. Zhao, X. Zhan, W. Zhang, P. Sang, Q. Wang, L. Tai, Q. Luo, Y. Li, C. Li and J. Chen, *J. Appl. Phys.*, 2022, **131**, 154101.

43 T. Maeda, B. Magyari-Köpe and Y. Nishi, 2017 IEEE International Memory Workshop (IMW), 2017, 1–4.

44 Y. Wu, Y. Zhang, J. Jiang, L. Jiang, M. Tang, Y. Zhou, M. Liao, Q. Yang and E. Y. Tsymbal, *Phys. Rev. Lett.*, 2023, **131**, 226802.

45 A. Silva, I. Fina, F. Sánchez, J. P. B. Silva, L. Marques and V. Lenzi, *Mater. Today Phys.*, 2023, **34**, 101064.